

FIG. 1 (a) The time evolution of the shape parameter ρ from the numerical simulation is shown as a function of time for different numbers of triangular mesh elements, n_f . (b) The error in the equilibrium shape parameter, ρ^{eq} , is plotted for different numbers of triangular elements on the surface. The value of ρ^{eq} at the finest grid size, $n_f = 740$, is taken as the exact value in computing the errors. (c) The shape of the precipitate is shown at the end of the simulation with 420 triangular elements. The parameters for all the figures are $V_0(\Omega^P) = 4\pi/3$, $Z = 6.4$, $\mu^P = 0.5$, $\mu^M = 1$, $\nu^P = \nu^M = 0.25$, and $\epsilon^T = \text{diag}(1, 1, 1)$.

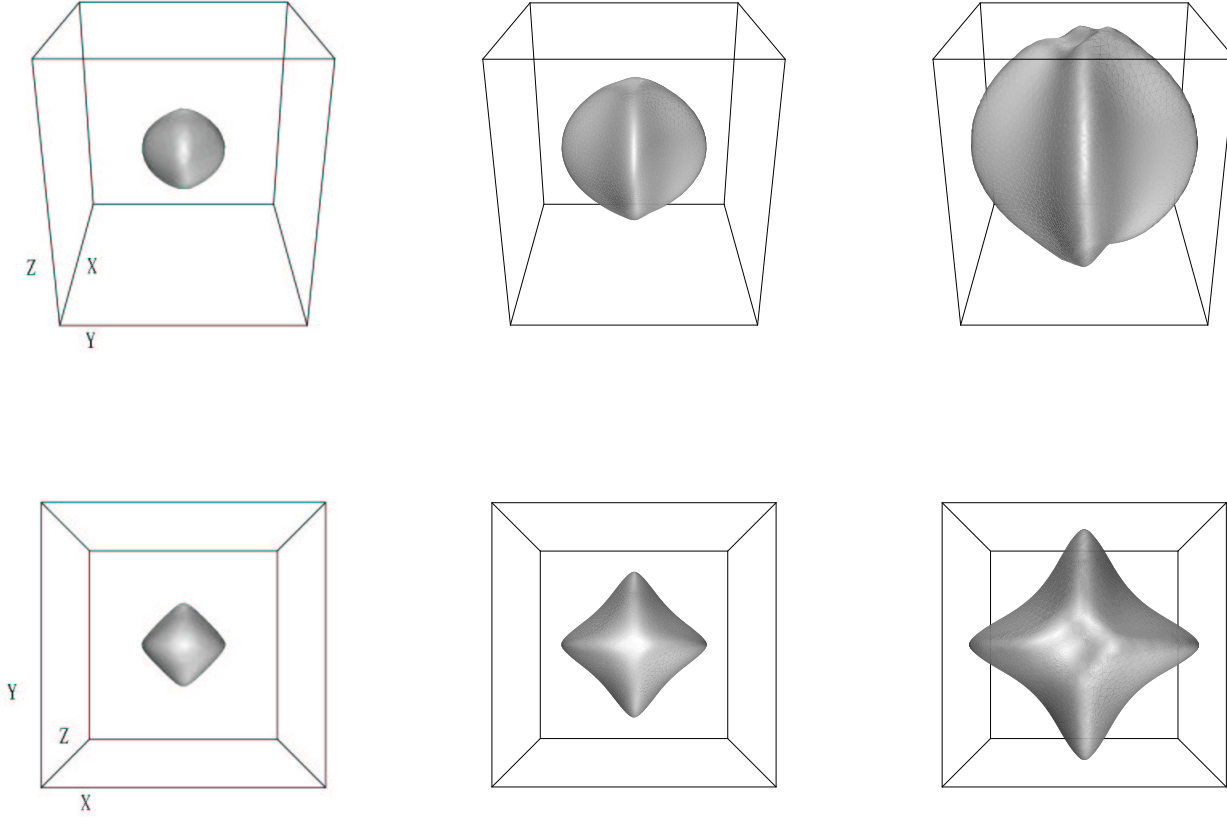


FIG. 2 Time sequence of precipitate shapes from a unit sphere with $J = 81$, $Z = 2$, elastic constants $\mu^P = 0.5$, $\mu^M = 1$, $\nu^P = \nu^M = 0.25$, and the misfit $\epsilon^T = \text{diag}(1, -1, 0)$. The top row shows three-dimensional views while the bottom row shows the same precipitates viewed from the positive z axis. The times for each column are $t = 0.18$, $t = 0.815$ and $t = 2.885$ (from left to right).

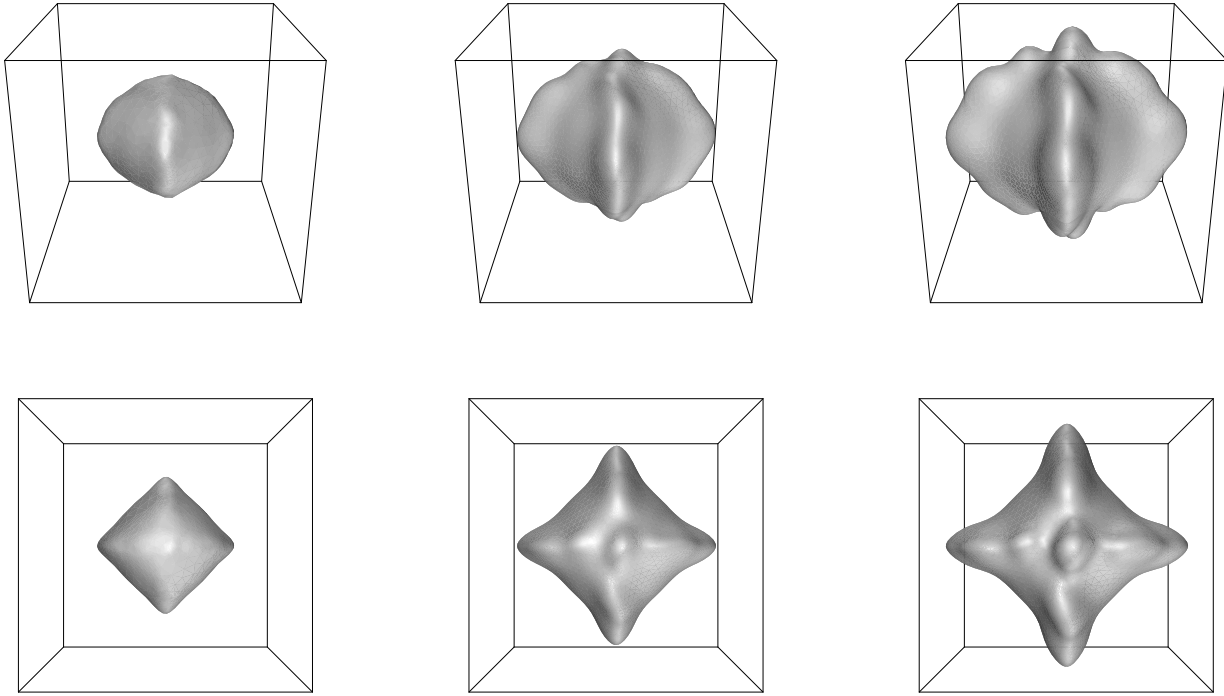


FIG. 3 Time sequence of precipitate shapes from a unit sphere with $c_\infty = -92.54$, $Z = 2$, elastic constants $\mu^P = 0.5$, $\mu^M = 1$, $\nu^P = \nu^M = 0.25$, and the misfit $\epsilon^T = \text{diag}(1, -1, 0)$. The views are the same as in figure 2. The times for each column are $t = 0.11$, $t = 0.18$ and $t = 0.25$.

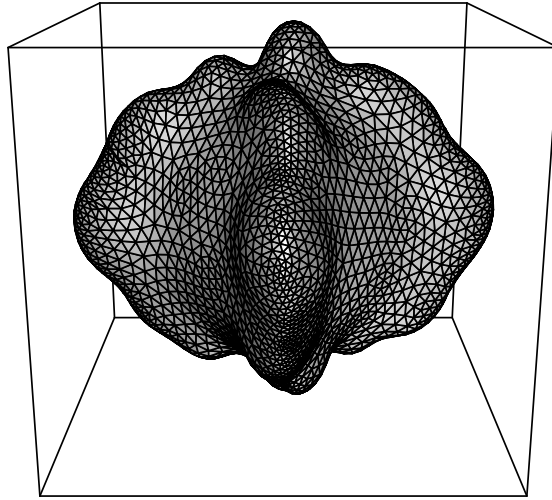


FIG. 4 The detailed mesh for the final shape ($t = 0.25$) of the constant far-field composition case shown in Fig. 3.

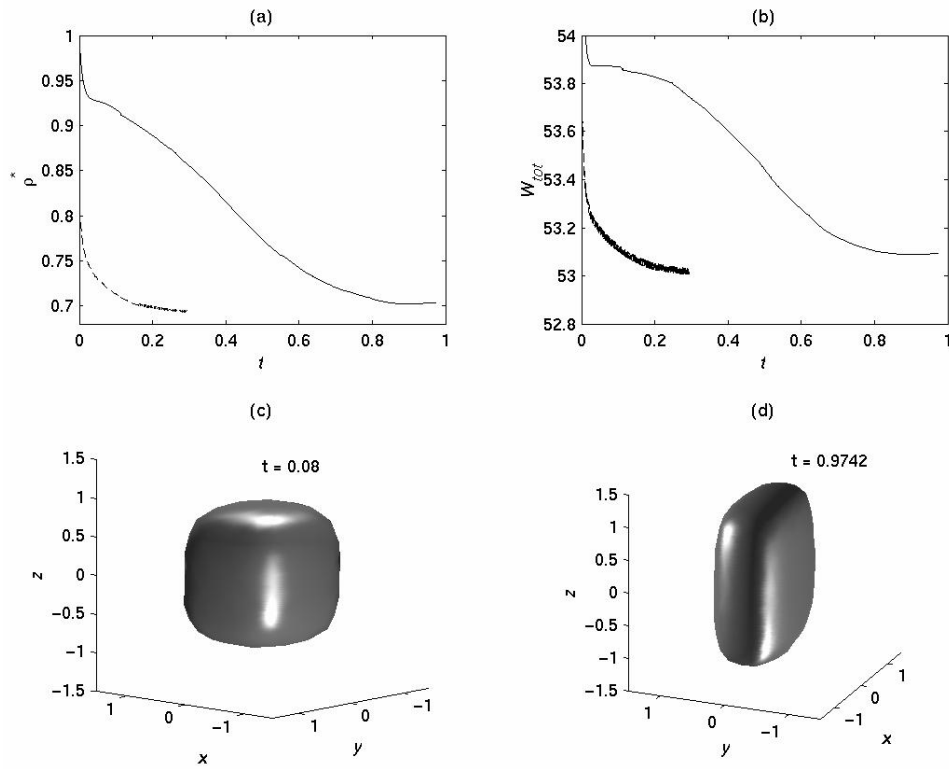


FIG. 5 (a) The evolution of the shape parameter ρ^* for a Ni_3Al precipitate in a nickel matrix. The solid line is obtained for evolution from a unit sphere, while the dashed line is from a spheroidal shape with the same volume. Also, the flux $J = 0$, $Z = 4$, and the misfit $\epsilon^T = \text{diag}(1, 1, 1)$. (b) The same as (a) except for the total energy W_{tot} . (c) The precipitate shape at time $t = 0.08$ as evolved from the unit sphere. (d) The precipitate shape at equilibrium.

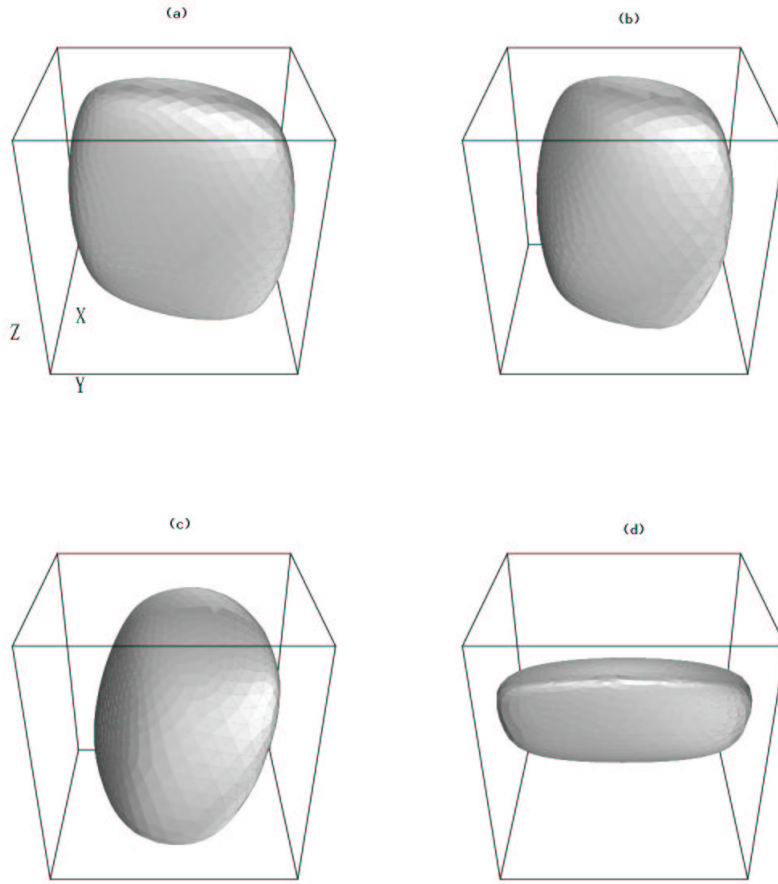


FIG. 6 The coarsened shapes of the Ni_3Al precipitates in nickel matrix as the crystallographic directions of the precipitate is rotated by an angle ξ in a plane with the normal $\mathbf{n} = \langle 0\bar{1}1 \rangle$. In (a), $\xi = 30^\circ$; (b), $\xi = 54.7^\circ$ and in (c), (d) $\xi = 90^\circ$. The precipitates in (c) and (d) were generated using different initial shapes as described in the text. In these simulations, $V_0(\Omega^P) = 4\pi/3$, $J = 0$, $Z = 4$ and $\epsilon^T = \text{diag}(1, 1, 1)$.

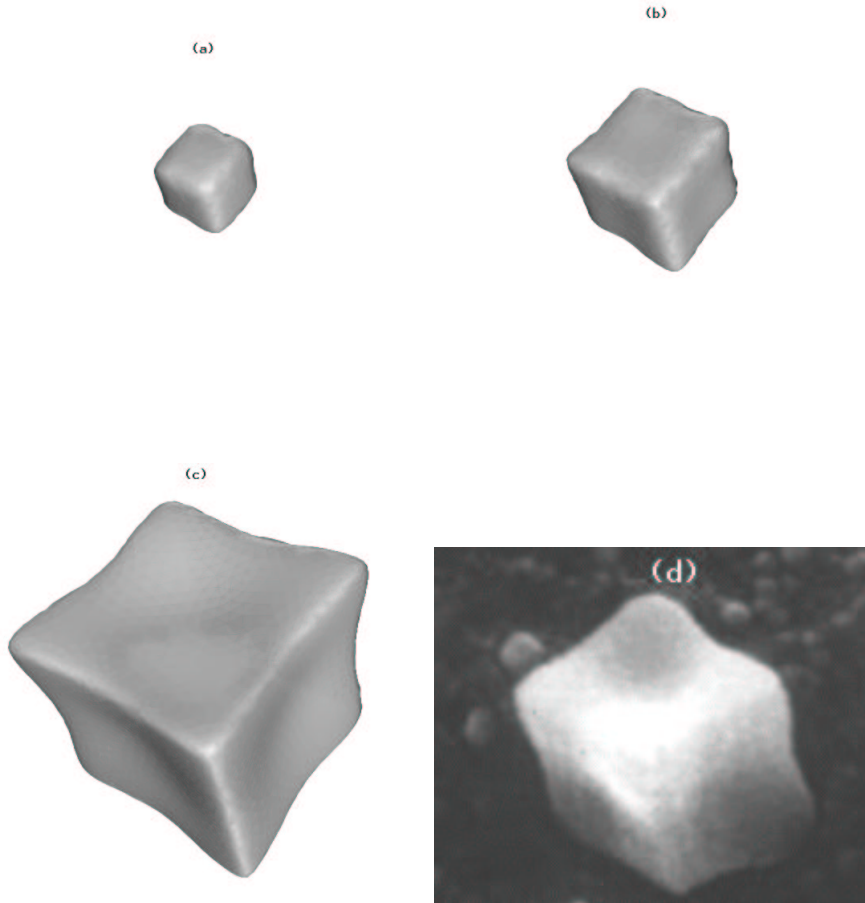


FIG. 7 Images (a)-(c) show a time sequence of the growth of Ni_3Al precipitates in a nickel matrix for the flux $J = 81$, $Z = 4$, and the misfit $\epsilon^T = \text{diag}(1, 1, 1)$. The initial shape is a unit sphere. The cubic axes are normal to sides of the growing cuboids so that the corners are in the cube diagonal directions. Figure (d) shows an image taken from an experiment [31] showing Ni-based precipitates with concave faces similar to those observed in our simulation.

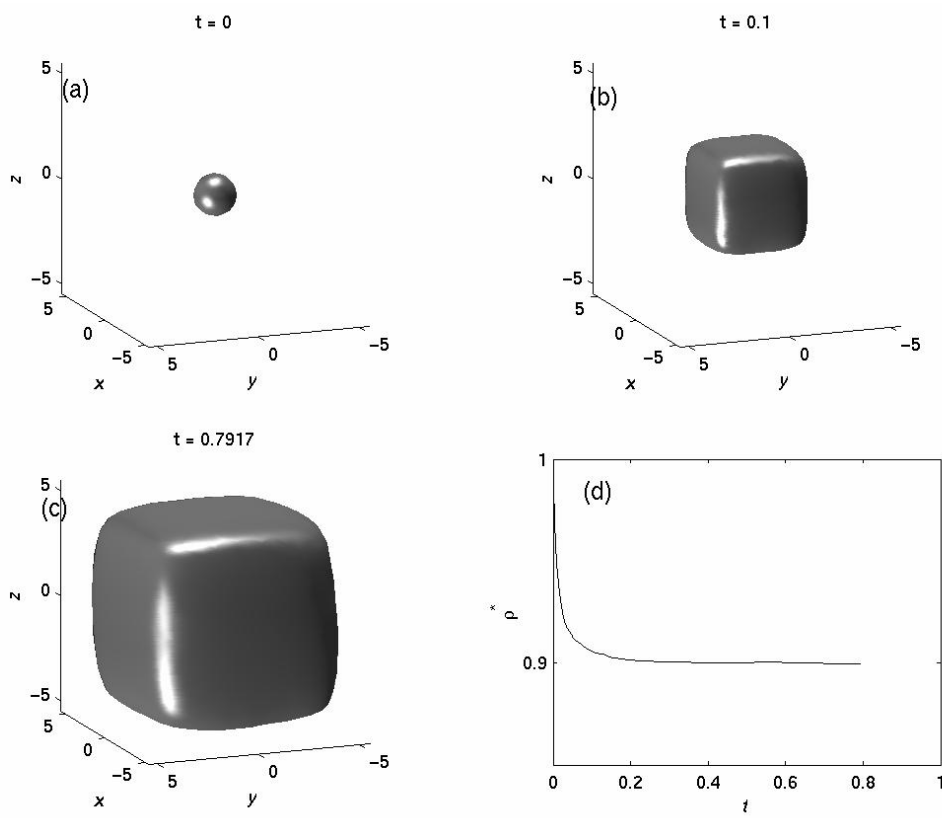


FIG. 8 Images (a)-(c) show a time sequence of the growth of a Ni_3Si precipitate in a nickel matrix for the flux $J = 81$, $Z = 4$, and the misfit $\epsilon^T = \text{diag}(1, 1, 1)$. The initial shape is a unit sphere. Figure (d) shows the corresponding evolution of the shape parameter ρ^* .